Revision 1

Word Count: 7453

Synthesis of Ferrian and Ferro-Saponites: Implications for the structure of (Fe,Mg)-smectites synthesized in reduced conditions

Hiroshi Sakuma [1,*], Koki Morida [2], Yoshio Takahashi [3], Keisuke Fukushi [2], Natsumi Noda [3,4], Yasuhito Sekine [2,4] and Kenji Tamura [1]

[1]*National Institute for Materials Science, 1-1, Namiki, Tsukuba, Ibaraki 305-0044*

[2]*Institute of Nature and Environmental Technology, Kanazawa University, Kakuma, Kanazawa 920-1192, Japan*

[3]*Department of Earth and Planetary Science, School of Science, University of Tokyo, Tokyo 113-0033, Japan*

[4]*Earth-Life Science Institute (ELSI), Tokyo Institute of Technology, 2-12-1IE-1, Ookayama, Tokyo 152-8550, Japan*

Corresponding author: H. Sakuma (SAKUMA.Hiroshi@nims.go.jp)

Abstract

Clay minerals are widely distributed on the surface of Earth, Mars, and Ceres in the Solar systems. Among clay minerals, smectites can record the history of the environment through exchange of interlayer cations with those in water, or through redox reactions with the atmosphere. Therefore, characterization of chemical compositions and crystal structures of smectites is crucial for revealing paleoenvironment. For instance, the crystal structure within octahedral sheets of iron-bearing smectites changes to trioctahedral sheets under reduced or dioctahedral sheets under oxidized conditions. Orbital infrared and X-ray diffraction (XRD) analyses by Mars orbiters/rovers revealed the presence of (Fe,Mg)-smectites on the surface of Mars; however, it has been difficult to characterize the properties of these (Fe,Mg)-smectites, which are rare on the surface of Earth. In this study, we synthesized ferrian (ferric ion-rich) and ferrous (ferrous ion-rich) (Fe,Mg)-saponite and revealed the effect of valence states and iron contents on the crystal structures. These saponites were synthesized using a hydrothermal method under reduced conditions. The crystal structures and valence states of iron were analyzed by XRD, Fourier-transform infrared spectroscopy, transmission electron microscopy, Mössbauer spectroscopy, and X-ray absorption near edge measurements. The synthesized clays were trioctahedral swelling clays and were identified as saponites. The valence state of iron in these synthesized saponites is altered by oxygen and a reducing agent in water; however, the trioctahedral structures are maintained under both oxidizing and reduced conditions, following a reversible reaction. This mechanism can be interpreted by the desorption and adsorption of hydrogen in the hydroxyls of the octahedral sheets of the smectite layers. The maximum basal spacing of the (02*l*) lattice plane in the octahedral sheets was defined by compiling various smectite data. When the basal spacing of (02*l*) is larger than the maximum in dioctahedral smectites, smectite can be identified as trioctahedral smectite. The redox state of iron in the octahedral sheet cannot be determined from the basal spacing of (02*l*). We revealed that the iron content in the trioctahedral sheet has a linear relationship with the length of the lattice parameter *b*. This provides a method to estimate the iron content in saponite from the XRD profile. The XRD profiles of smectites found at the Yellowknife Bay on Mars can be explained only by trioctahedral smectites, and the iron content in the octahedral sheet is roughly estimated to be 0.5–1.7 in a half-unit cell. These results indicate that the presence of (Fe,Mg)-saponite implies a reduced environment during the formation and that this iron-bearing saponite has oxidation and reduction capabilities depending on the environment.

Keywords: Reduction, oxidization, smectites, XRD, XANES, clay mineralogy, Mars

Introduction

Clay minerals are widely distributed on the surface of Earth (e.g., Fagel 2007), Mars (e.g., Ehlmann et al. 2011; Carter et al. 2013; Michalski et al. 2015; Bishop et al. 2018), and Ceres, the icy dwarf planet in the main belt (e.g., De Sanctis et al. 2015, 2020; Ammannito et al. 2016). Among these clay minerals, (Fe,Mg)-smectites that are commonly discovered play an important role in understanding the history of Mars. Owing to their high affinity for water, smectites, and in particular, their chemical compositions and exchangeable interlayer cations may record the history of the Martian paleoclimate (e.g., Fukushi et al. 2019). Moreover, the valence state of iron in smectite is one of the key properties for revealing the redox state during smectite formation.

Visible/near-infrared (VNIR) spectra measured by Martian orbital instruments may be used to identify the valence state of iron in smectite. It has been recently revealed that the VNIR spectra of the synthesized ferrous (Fe^{2+}) saponite could be distinguished from those of ferric dioctahedral smectite (such as nontronite) (Chemtob et al. 2015). The oxidation state of octahedral iron in smectites with a wide range of chemical compositions, including Fe(III), Fe(II), Mg, and Al, can also be identified from the VNIR spectra (Fox et al. 2021). These studies provide critical data for the identification of ferrous smectites in VNIR spectra. On the current surface of Mars, however, detectable ferrous smectites are likely limited possibly due to oxidative chemical weathering in sediment sources and/or during fluvial transports (Bristow et al. 2018; Mangold et al. 2019), and photochemically produced oxidants (Chemtob et al. 2015, 2017).

Nevertheless, unoxidized samples below the surface can be found by a rover. For example, X-ray diffraction (XRD) data for samples below the surface were provided by the Chemistry and Mineralogy (CheMin) instrument onboard the Curiosity rover at Yellowknife Bay (YKB) (Vaniman et al. 2014). It is believed that the redox state can be revealed for the octahedral structures of smectites, because the divalent cations fully occupy these sites, called a trioctahedral sheet, while the trivalent cations, owing to the charge balance, can occupy only two-thirds of these sites, called a dioctahedral sheet. This difference in the structure of the octahedral sheets can be identified by X-ray diffraction (XRD) of the (060) plane in the smectite. The 060 reflection, however, cannot be measured by the CheMin instrument; instead, the 02*l* reflections were used to identify the octahedral structures in the spectra obtained by the CheMin (Treiman et al. 2014; Vaniman et al. 2014; Bristow et al. 2015).

A natural trioctahedral smectite (ferrian saponite) on Earth can be used as equivalent to explain the 02*l* peak position of clays at YKB; however, surprisingly, most iron in natural saponite was characterized as ferric (Fe^{3+}) (Treiman et al. 2014), which is expected to be unstable in the trioctahedral sheet. The synthesized ferrous (Fe^{2+}) saponite can also be a candidate for understanding the structure of YKB smectites (Chemtob et al. 2015; Fox et al. 2021) from XRD profiles. These results imply that the structure of the octahedral sheet may not be used to identify the oxidation state of iron; however, it is unclear why the ferric ions are stable in the trioctahedral sheet. These studies were conducted on highly oxidized or reduced saponites. The results imply that the intermediate ratio of ferric and ferrous ion may also explain the smectites at YKB.

In this study, we attempted to synthesize ferrian (ferric-ion-rich) and ferro (ferrous ion-rich) saponites. These saponites were used to reveal the possibility of constraining the oxidation state of iron in saponite from the XRD profile and to interpret the mechanism of stabilization of ferric ion in trioctahedral smectite. Two hydrothermal synthetic methods have been proposed for obtaining ferrous saponite under reduced conditions. One is a sol-gel method in an anoxic chamber (Chemtob et al. 2015, 2017; Fox et al. 2021), while the other method used a reducing agent in aqueous solutions (Baldermann et al. 2014). In this study, we employed the latter method. The difference with the previous work

(Baldermann et al. 2014) is the presence of Al in the reactants; therefore, the details of the method were slightly modified. The Fe/Mg ratio in the starting materials was fixed at one as the upper limit of the trioctahedral smectite measured by the Curiosity rover (Vaniman et al. 2014). The ratio of ferric/ferrous ion in the saponite was controlled by oxidation and reduction of synthesized saponite, as reported for dioctahedral smectites (Stucki et al. 1984; Fialips et al. 2002; Lee et al. 2006).

Materials and Methods

Synthesis of iron saponite

The synthetic method was similar to that of ferrous saponite synthesis proposed by Baldermann et al. (2014). The reducing agent was prepared by adding 0.025 g sodium dithionite ($Na_2S_2O_4$) to 50 mL ultrapure water (resistivity of 18.2 MΩ cm). Initial solutions were obtained by adding 2 g of sodium orthosilicate (Na_4SiO_4), iron (II) sulfate ($FeSO_4$ $7H_2O$), magnesium chloride ($MgCl_2$ $6H_2O$), and $AlCl_3$ ($AlCl_3$ $6H_2O$) powders of reagent grade to the reducing agent to meet the desired stoichiometry (Table 1). The difference among samples is the concentrations of Al and Si in the initial solutions. The concentrations of Al in FS007, FS009, and FS010 were prepared to satisfy the stoichiometry of 0.5, 0.3, and 0 (/O_{12} in the chemical formula of saponite), respectively. The Si concentrations in these samples were determined to satisfy the sum of Al and Si concentrations to be four (/O_{12}). The pH of the initial solutions was 12.7, which was higher than that of the previous method (Baldermann et al. 2014). This high pH prevents the precipitation of Al hydroxide from the solution. The solutions were transferred to Teflon-lined stainless-steel autoclaves and heated in an oven at 180 °C for five days. The solutions were cooled to room temperature within a few hours, and precipitates were obtained by vacuum filtration on a 0.45 μm PTFE membrane filter. The precipitates on the filter were rinsed with ultrapure water to remove residual salts and dried at 40 °C in an oven.

To obtain ferro-saponite, the reduction was attempted using a method similar to that proposed for di-octahedral smectites (Stucki et al. 1984; Fialips et al. 2002; Lee et al. 2006). The recovered sample (150 mg) was dispersed in 100 mL of ultrapure water for one–five days. The suspension (40 mL) was mixed with 20 mL of buffer solution by combining 2 parts of 1.2 M sodium citrate with 1 part of 1 M sodium bicarbonate. This suspension was moved to a glove box, and the air was replaced with N_2 gas. Then, 300 mg sodium dithionite was added to the suspension and heated at 70 °C for 1 h or 24 h. The suspension was transferred to a centrifuge tube and centrifuged at 18,000 rpm for 15 min, followed by one wash with methanol under centrifugation. Then, the supernatant was discarded, and the precipitate was dried in a vacuum desiccator.

Chemical analysis

The synthesized sample (25 mg) was dissolved in a mixture of 5 mL of 35% nitric acid and 0.5 mL of hydrofluoric acid at 120 °C for 16 h, allowed to cool, and diluted to 250 mL with Milli-Q water. The concentrations of elements (Na, Mg, Al, Si, S, K, Ca, and Fe) were measured using an SPS3520UV-DD-type inductively coupled plasma optical emission spectrometry (ICP-OES) instrument (Hitachi High-Tech Corp.). The chemical composition of the synthesized samples was also analyzed using a field-emission electron microscope (JEM-3100FEF, JEOL Ltd.) in scanning mode equipped with an SDD detector for energy dispersive X-ray spectroscopy (STEM-EDS). The samples were prepared on carbon grids. An accelerating voltage of 300 kV was applied for electron microscopy.

The structural formulas for the synthesized smectites were calculated as follows: (1) The sum of positive charges was calculated from the molar ratio of the cations. (2) The number of cations in the half-unit cell was calculated by normalizing the total positive charge to compensate for 22 units of negative charge. (3) Based on the number of cations, cations were assigned to smectite structures. All Na atoms were assigned to the interlayer. All Si and

Al atoms were assigned to the tetrahedral sheet, because Al^{3+} preferentially occupy tetrahedral sites in saponite (He et al. 2014). All Mg atoms were assigned to the octahedral sheet. Fe was assigned to the octahedral sheet as ferrous ions until the full occupancy of three ions per half-unit cell was reached. Residual Fe was assigned to the tetrahedral sheet as ferric ions. In this procedure, the sum of positive charge changes depended on the ratio of ferrous/ferric ions; therefore, the ratio was determined iteratively to satisfy the full occupancy of the octahedral sheets by Mg and Fe ions.

The valence states of Fe ions in the samples were analyzed by X-ray absorption near edge structure (XANES) measurements. Iron K-edge XANES spectra were measured at beamline BL12C at the Photon Factory (PF), Institute of Materials Structure Science, High Energy Accelerator Research Organization (KEK), Tsukuba, Japan. Incident X-ray beam was monochromatized with a Si-111 double-crystal monochromator and focused to 0.5×0.5 mm^2 with a bent cylindrical mirror. Energy calibration was performed by defining the pre-edge peak maximum of hematite fixed at 7.110 keV. The measurements were performed at room temperature under ambient air conditions. All spectra were recorded in the transmission mode using two ion chamber detectors. All spectra were normalized to a unit step in the absorption coefficient. No radiation damage that caused a change in the valence of Fe was found during the data acquisition based on the repeated scans for the XANES analysis. The XANES spectra of two typical clay minerals were measured for a comparison. Pure biotite was purchased from Nichika Inc. and the ratio of ferric ions is low ($Fe^{3+}/\Sigma Fe = 0.03$). Nontronite (NAu-1) is a source clay of the Clay Minerals Society.

Iron speciation in some of the saponite and biotite samples were also conducted by Mössbauer (MB) spectroscopy. The powdered sample without any chemical pretreatment was gently pressed into a brass sample holder (16 mm in diameter, 1 mm thick) for the measurement. MB spectra were measured using a Topologic Systems MFD-110D spectrometer with a 57Co/Rh source at room temperature. The Doppler velocity was set to the range between −10 to 10 mm/s to cover sextet peaks. Isomer shifts were defined with respect to the centroid of the spectrum of a metallic iron foil. The obtained spectra were fitted to Lorentzian line shapes using a least-squares method with restrictions of half-width (HW) and peak intensity of each quadruple doublet constrained to be equal. The range of fitting parameters were constrained to be consistent with those reported for clay minerals (Johnston and Cardlie. 1978; Vandenberghe and Grave. 2013). A least squares fitting was conducted by using the program *MossA* (Prescher et al. 2012). The relative content of each iron species was calculated from the peak area determined by the fitting of three doublets corresponding to the ferrous ion, ferric ion in octahedral and tetrahedral sites. These areas were corrected by a recoilless fraction ratio of 1.21 as the ferric to ferrous ions (De Grave and Van Alboom. 1991; Morris et al. 1995).

Identification of mineral species

The mineral species of the samples were analyzed by X-ray diffraction (XRD) and Fourier-transform infrared (FT-IR) methods. The XRD profiles were measured under dry conditions (relative humidity <2%) in a chamber filled with N_2 gas using an Ultima IV instrument (Rigaku). X-rays were emitted from a Cu Kα source (wavelength: 0.15418 nm) at 40 kV and 30 mA. The scanning speed was 4 °/min with a step size of 0.02 °. The XRD profiles of some typical smectites were measured for a comparison. Montmorillonite (Kunipia-F) and saponite (Smecton SA) were the source clays of the Clay Science Society of Japan and these were purchased from Kunimine Industries Co., Ltd. The FT-IR spectra were obtained in the attenuated total reflectance (ATR) mode using an IRAffinity-1 instrument (Shimadzu Corp.) over the range of 400−4000 cm^{-1}. The morphology and crystal structures of the samples were analyzed by transmission electron microscopy (TEM) and electron diffraction (ED) using a JEM-3100FEF JEOL microscope. The samples were prepared on carbon grids. An accelerating voltage of 300 kV was applied.

Results and discussion

Mineral species in precipitates

The XRD profiles of the precipitates are shown in Figure 1. Typical smectites are also plotted for comparison. These precipitates show characteristic reflections of 2:1-type clay minerals as 001 at d-spacings (*d*) of ~11–15 Å, for 02*l* and 11*l* reflection *d* = 4.57–4.59 Å, for 20*l* and 13*l* *d* = 2.59–2.63 Å, and for 060 *d* = 1.54 Å. The shift in the 00*l* peaks as a function of relative humidity (not shown here) indicates that these minerals are smectite. The 060 reflection at *d* = 1.54 Å is clearly larger than those of dioctahedral smectites (nontronite and montmorillonite); therefore, these synthesized smectites are categorized as trioctahedral smectite such as Mg-saponite. No clear difference was observed among the synthesized samples (FS007, 009, and 010), although some impurities of hematite were identified in the FS007 sample. Such impurities can be formed because of the insufficient removal of oxygen from the initial solution. The difference in the 001 peak position depended on the dry state before the XRD measurements. The swelling behavior will be studied in future work.

The FT-IR spectra of the precipitates are shown in Figure 2. The low frequency of the Si-O stretching band at 950 cm^{-1}, the O-H bending band at 650 cm^{-1}, and a single main maximum at ~420 cm^{-1} indicate that the precipitants are typical trioctahedral clays (Russell and Fraser 1994). The position of the Si-O stretching band was lower than that of a common saponite (~1000 cm^{-1}). This can be interpreted as the presence of Fe^{3+} tetrahedral sites substituted for Si (Goodman et al. 1976). The difference in Al content can be identified by the absorbance at ~740 cm^{-1}. This wavenumber has been interpreted by tetrahedral Al-O-Si in-plane vibrations (Russell and Fraser 1994) indicating that the Al ions substitute for Si in tetrahedral sheets. The absorptions at 1640 and ~3400 cm^{-1} correspond to the bending and stretching modes of the interlayer water, respectively. The IR band at ~3600 cm^{-1} can be attributed to the stretching mode of the octahedral metal (M = Mg or Fe) ions and the OH group (M_3OH). The frequency can be interpreted by the presence of Fe ions in the trioctahedral sheets as observed for iron-rich biotite. The broad and low frequency of the band may be interpreted as the presence of some OH groups in a locally dioctahedral environment such as vermiculite (Russell and Fraser 1994).

Chemical compositions of trioctahedral smectites

The chemical compositions of the precipitates analyzed by ICP-OES are listed in Table S1**.** The chemical compositions of the oxides are listed in Table 2. The calculated chemical formulas of the trioctahedral smectites are listed in Table 3. The chemical formula of FS007 was not calculated because of the presence of hematite and magnetite in the sample. The layer charge of FS009 (−0.86) calculated from the summation of charge without Na ions is larger than the charge of interlayer Na ions (+0.54) to neutralize the charge. This may be attributed to the presence of ferric ions in the octahedral sheets. Based on the XRD and FT-IR analyses, as well as on the chemical compositions of the precipitates, the synthesized crystals were identified as trioctahedral iron saponites.

Oxidation and reduction

To obtain ferrian saponite, trioctahedral iron saponite (FS009) was oxidized by dispersing it in water for one day. The XRD patterns of the dried samples (FS009O) are shown in Figure 3. There is no clear difference from the original saponite (FS009) in the reflections assigned to smectite by oxidation. Some reflections from magnetite and hematite in the sample (FS009O) appeared after oxidation. The *d*-spacing of the 060 reflection was 1.54 Å, indicating that the smectite was still trioctahedral saponite after oxidization. The TEM images and ED patterns of FS009O are shown in Fig. 4(a)–(c). The ED patterns of the low-resolution TEM area are characterized by diffraction from smectites. A clear layered structure was observed with a thickness of ~1 nm. These analyses indicate that the major mineral in FS009O is trioctahedral smectite.

Iron saponite was reduced to obtain ferro-saponite. The XRD profiles in Fig. 3 show no difference from FS009O in the reflections assigned to saponite, but the reflections from magnetite and hematite disappeared. No significant difference in the reduction time was observed between 1 and 24 h. The TEM images and the ED patterns of FS009R1h, as shown in Figure 4 (d) –(f), indicate that the reduction did not change the morphology. The difference compared to the FS009O sample was the disappearance of impurities observed in the ED profiles of FS009O, as expected from the XRD profiles.

The XANES spectra of reduced (FS009R24h and FS009R1h) and oxidized (FS009O) FS009 samples are shown in Figure 5 with biotite and nontronite (NAu-1) as endmembers of ferrous and ferric clay minerals for a comparison. Most iron in biotite and nontronite can be assigned to ferrous and ferric ion, respectively. The shape of FS009O was similar to that of NAu-1, while those of FS009R24h and FS009R1h were similar to that of biotite, indicating that the valence and coordination environment of iron changed by reduction from ferric to ferro-saponites. The edge position defined at the normalized absorbance of 0.5 roughly corresponds to the ratio of ferric and ferrous ions (Chemtob et al. 2015, 2017). The edge positions shown as open circles in Figure 5 change from high to low energy by reduction. The energies in the spectra of the reduced saponites (FS009R1h and FS009R24h) were clearly higher than that of biotite, indicating that these saponites are not perfect ferrous saponite but rather ferro-saponite. A rough estimation of $Fe^{3+}/\Sigma Fe$ was conducted, as listed in Table 4, following the previous linear fitting method (Chemtob et al. 2015, 2017) under the assumptions that $Fe^{3+}/\Sigma Fe = 1$ for NAu-1 and 0 for biotite. The estimation of uncertainty in this linear fitting method is difficult, but the uncertainty can be ±0.06 from the difference in two spectra of biotite measured on different days; therefore, the difference between FS009R1h and FS009R24 (0.06) may not be significant, indicating that the 1-h reduction is sufficient to reach equilibrium in the reduction state.

The MB spectra of reduced (FS009R24 and FS009R1h) and oxidized (FS009O) FS009 samples are presented in Figure 6 with biotite for a comparison. The fitting parameters are listed in Table 5. The measurements were conducted for a small amount of available samples of saponites after several months since these saponites were synthesized; therefore, oxidation may progress more than the samples analyzed by the XANES spectra. The signal to noise (S/N) ratio in the MB spectrum of FS009O was low; therefore, the two doublets representing octahedral ferric and ferrous ion were used for the fit. The spectra of fresh biotite showed sufficient S/N ratio and it can be explained by ferrous ions. Estimated $Fe^{3+}/$

Σ Fe ratio (0.09±0.04) is consistent with the 0.03 estimated by a titration measurement reported by Nichika Inc. Reduced saponites (FS009R1h and FS009R24h) can be explained by the mixed sites of ferrous ion, ferric ion in octahedral and tetrahedral sites. Uncertainties are large, but approximately 10% tetrahedral ferric ion can be present in both saponites. The spectrum of oxidized saponite (FS009O) was mostly explained by the ferric ion. The presence of tetrahedral Fe^{3+} can be interpreted by the high pH (12.7) of the initial solutions as reported in Baron et al. (2016). They confirmed that the Fe^{3+} content in tetrahedral sheet in smectite increases with increasing the pH at the end of the synthesis. In our experimental conditions, perfect reduced conditions may not be hold during synthesis and the Fe^{3+} ion were incorporated in the tetrahedral sheets.

A comparison of estimated $Fe^{3+}/\Sigma Fe$ ratio between XANES and MB spectra is presented in Figure 7. Note that the error bars of XANES results would be a minimum because the error was estimated from the variation of two biotite samples. There is a difference in absolute values between the XANES and MB results; however, the tendency is similar. Several reasons of the difference in the absolute values can be considered such as the linear fitting in XANES spectra, the empirical value of recoilless fraction ratio in MB spectra, and oxidation of saponite samples before the MB measurements. Here we assume that the estimates by XANES and MB spectra are the minimum and maximum estimates in the synthesized saponites, respectively.

The estimates for FS009R24h and FS009R1h indicate that 30% of the ferric ions cannot be reduced by the reduction method in this study. These ferric ions may be stable in tetrahedral sheets, because the pre-edge peaks at ~7112 eV, the typical peak of iron in tetrahedral sites, were clearly observed in these samples (Wilke et al. 2001). From the analysis of MB spectra, approximately 10% of ferric ion can be present in the tetrahedral sites. In FS009O, 15-30% of the ferrous ions cannot be oxidized which is consistent with the oxidation of ferrous saponite in air oxidation experiments (Chemtob et al. 2017). These ferrous ions may be stable in the trioctahedral sheets stabilized by Mg ions. Further oxidation can occur in H_2O_2 solutions which has a higher redox potential than O_2; however, this oxidation makes the ejection of ferric ions from the octahedral sheets and the octahedral sheets transforms to a dioctahedral structure (Chemtob et al. 2017).

We attempted to measure the valence state of iron in our small samples using electron energy loss spectroscopy (EELS) in TEM; however, it was impossible to remove the effect of electron irradiation-induced oxidation, as confirmed for silicate perovskite (Lauterbach et al. 2000). Most clay samples, including biotite, were damaged by the electron beam, and the peaks of the EELS spectra shifted to that of Fe^{3+}, similar to that observed in the previous work. Such a change did not occur in the synthesized ilmenite ($Fe^{2+}TiO_3$) samples.

Implications

Possibility to identify the smectite species and Fe content by 02*l* reflection

The detailed XRD profiles around 02*l* reflections of the synthesized ferrian (FS009O) and ferro-saponites (FS009R24h) are presented in Figure 8. To compare our samples with those measured at the YKB in the Gale crater (Vaniman et al. 2014), the 2θ angle was recalculated using the wavelength of a Co-Kα X-ray source. These ferrian and ferro-saponites can explain the 02*l* reflections of smectites found at the YKB, as reported for Griffith Park ferrian saponite (Treiman et al. 2014). This indicates that the current oxidation states of iron in the octahedral sheet could not be determined from the XRD profile. The question remains whether the Fe content in the smectite can be determined from the XRD profile.

A linear correlation between the lattice parameter *b* and Fe content has been confirmed in octahedral sheets of dioctahedral smectites (Eggleton 1977; Brigatti 1983). In most cases, the *b* values were calculated from the 060 reflections; therefore, the linear correlation holds between the *d* spacings of the 060 reflections (d_{060}) and the Fe contents (Köster et al. 1999). The question is whether this relationship still holds for d_{02l} values because there is no data for d_{060} for the YKB samples. Moreover, this correlation was not confirmed for trioctahedral smectites.

The relationships between d_{060} and d_{02l} in our results and those of previous studies (Nagelschmidt 1938; Earley et al. 1952; Sudo 1954; Weir and Greene-Kelly 1962; Eggleton 1977; Brigatti 1983; Köster et al. 1999; Miyawaki et al. 2010; Baldermann et al. 2014; Treiman et al. 2014; Chemtob et al. 2015; Fox et al. 2021) are shown in Figure 9. A linear relationship was confirmed between d_{060} and d_{02l}, although the d_{02l} value is slightly smaller than that calculated by $3d_{060}$, which is shown as a solid line. This trend was reported for the synthesized iron smectite, with the small values of d_{02l} interpreted as a result of turbostratic disorder in smectites (Fox et al. 2021). In these smectites, the maximum intensity of 020 does not necessarily coincide with that of d_{020} (Moore and Reynolds, Jr 1997). Even after considering the effects of turbostratic disorder in smectites, the shaded d_{02l} of smectite at YKB can only be explained by trioctahedral smectite.

The Fe contents in the octahedral sheets are plotted in Figure 10 as a function of the lattice parameter *b* calculated from d_{060}. As reported in previous studies (Eggleton 1977;

Brigatti 1983), a linear relationship can be confirmed for dioctahedral smectites (dashed lines fitted to open symbols), although the deviation is large for iron-rich montmorillonite (Fox et al. 2021). This deviation can be attributed to the presence of Mg ions in the octahedral sheets. The ionic radius of a Mg ion in a six-coordinated state (0.72 Å) is larger than that of a ferric ion (0.65 Å), and both are larger than that of an Al ion (0.53 Å) (Shannon and Prewitt 1969); therefore, the increased fraction of Mg ions in the dioctahedral sheets of these minerals increases the *b* value, though the Fe content is low.

Such a linear relationship seems to hold for trioctahedral smectites (solid line fitted to solid symbols in Fig. 10). The deviation of di-trioctahedral Fe smectite and Fe saponite (Fox et al. 2021) can be explained by the presence of small Al ions in the octahedral sheet. As the *b* value of smectites at the YKB can be estimated to be 9.18–9.27 Å from the plausible d_{060} values (1.53–1.545 Å) in Figure 9, the Fe content in the octahedral sheets can be 0.5–1.7 in a half unit cell, as calculated by the solid line. This is a rough estimate, and the range should be refined by constraining the chemical compositions in octahedral sheets and by increasing the statistical confidence level by collecting more data on synthesized trioctahedral samples.

A plausible mechanism of stable trioctahedral sheets occupied by trivalent ferric ions

The high d_{060} values of oxidized and reduced smectites indicate that the octahedral sheet keeps the trioctahedral structure through these redox states and most octahedral sites are occupied by cations. From the point of charge neutralization, the substitution of O^{2-} for OH^{-} in the structure may occur during oxidization (Treiman et al. 2014). From the ideal chemical composition of ferrous saponite ($Na_{0.5}(Mg_{2.0}Fe_{1.0})(Si_{3.5}Al_{0.5})O_{10}(OH)_2$), we consider the following oxidation reaction:

$$2Na_{0.5}(Mg_{2.0}Fe_{1.0}(II))(Si_{3.5}Al_{0.5})O_{10}(OH)_2 + 0.5O_2 \rightarrow$$

$$2Na_{0.5}(Mg_{2.0}Fe_{1.0}(III))(Si_{3.5}Al_{0.5})O_{11}(OH) + H_2O$$

If this reaction is possible, desorption of hydrogen should occur without destruction of the octahedral sheets during oxidization. On the other hand, the incorporation of hydrogen in the structure may occur during the reduction process; therefore, the reaction can be reversible. This reaction occurs in trioctahedral biotite and vermiculite (Farmer et al., 1971). The synthesized ferrous saponite can be oxidized in water as FS009O, and this ferrian saponite can be reduced to FS009R1h. The reaction is reversible, which supports the hypothesis. The maximum number of hydrogen atoms in this formula is two; therefore, this limits the maximum number of ferrous ions in the octahedral sheet to two in this formula.

The Fe content in the octahedral sheet of the studied samples is less than the maximum; therefore, all ferrous ions in the octahedral sheet can be oxidized.

To verify the above discussion, the chemical compositions of FS009O and FS009R1 were estimated using STEM-EDS and the $Fe^{3+}/\Sigma Fe$ ratios listed in Table 4. Selected chemical compositions of these smectites (FS009O and FS009R1h) estimated by STEM-EDS are listed in Table S2. This analysis can omit impurities such as magnetite and hematite due to a small beam spot, and it may reflect the local composition if the composition is heterogeneous. Here, the average chemical compositions from three analyzed points were used for the following discussion. The chemical formula of these saponites was determined as follows: (1) The initial chemical formula was determined using the STEM-EDS data, similar to the procedure described for the ICP-OES data. (2) All ferrous ions estimated from Table 4 were assigned as octahedral iron. The residual iron in the octahedral sheet is assigned to ferric ions. (3) To neutralize the charge, the number of H atoms was adjusted. The calculated chemical formulae are presented in Table 6. The number of H atoms in FS009O was clearly smaller than that in FS009R1h. This may support the mechanism of the oxidation reaction through desorption of H.

Acknowledgements and Funding

We would like to thank M. Mitome, K. Kurashima, and Y. Owada (NIMS) for operating and interpreting the TEM observations, and A. Iwanade (NIMS) for his assistance with the wet chemical analysis. Comments on the experiments by K. Hashi (NIMS) were also appreciated. This work was supported by JSPS KAKENHI (Grant Number JP17H06458).

References

Ammannito, E., DeSanctis, M.C., Ciarniello, M., Frigeri, A., Carrozzo, F.G., Combe, J.-P., Ehlmann, B.L., Marchi, S., McSween, H.Y., Raponi, A., and others (2016) Distribution of phyllosilicates on the surface of Ceres. Science, 353, aaf4279, 7pp.

Baldermann, A., Dohrmann, R., Kaufhold, S., Nickel, C., Letofsky-Papst, I., and Dietzel, M. (2014) The Fe-Mg-saponite solid solution series – a hydrothermal synthesis study. Clay Minerals, 49, 391–415.

Baron, F., Petit, S., Tertre, E., and Decarreau, A. (2016) Influence of aqueous Si and Fe speciation on tetrahedral Fe(III) substitution in nontronites: A clay synthesis approach. Clays and Clay Minerals, 64, 230-244.

Bishop, J.L., Fairén, A.G., Michalski, J.R., Gago-Duport, L., Baker, L.L., Velbel, M.A., Gross, C., and Rampe, E.B. (2018) Surface clay formation during short-term warmer and wetter conditions on a largely cold ancient Mars. Nature Astronomy, 2, 206–213.

Brigatti, M.F. (1983) Relationships between composition and structure in Fe-rich smectites. Clay Minerals, 18, 177–186.

Bristow, T.F., Bish, D.L., Vaniman, D.T., Morris, R. V., Blake, D.F., Grotzinger, J.P., Rampe, E.B., Crisp, J.A., Achilles, C.N., Ming, D.W., and others (2015) The origin and implications of clay minerals from Yellowknife Bay, Gale crater, Mars. American Mineralogist, 100, 824–836.

Bristow, T.F., Rampe, E.B., Achilles, C.N., Blake, D.F., Chipera, S.J., Craig, P., Crisp, J.A., Des Marais, D.J., Downs, R.T., Gellert, R., and others (2018) Clay mineral diversity and abundance in sedimentary rocks of Gale crater, Mars. Science Advances, 4, eaar3330, 8 pp.

Cahoon, H.P. (1954) Saponite near Milford, Utah. American Mineralogist, 39, 222–230.

Carter, J., Poulet, F., Bibring, J.P., Mangold, N., and Murchie, S. (2013) Hydrous minerals on Mars as seen by the CRISM and OMEGA imaging spectrometers: Updated global view. Journal of Geophysical Research E: Planets, 118, 831–858.

Chemtob, S.M., Nickerson, R.D., Morris, R. V, Agresti, D.G., and Catalano, J.G. (2015)

Synthesis and structural characterization of ferrous trioctahedral smectites: Implications for clay mineral genesis and detactability on Mars. Journal of Geophysical Research: Planets, 120, 1119–1140.

Chemtob, S.M., Nickerson, R.D., Morris, R. V., Agresti, D.G., and Catalano, J.G. (2017) Oxidative Alteration of Ferrous Smectites and Implications for the Redox Evolution of Early Mars. Journal of Geophysical Research: Planets, 122, 2469–2488.

De Grave, E., and Van Alboom, E. (1991) Evaluation of ferrous and ferric Mössbauer fractions. Physics and Chemistry of Minerals, 18, 337-342.

De Sanctis, M.C., Ammannito, E., Raponi, A., Marchi, S., McCord, T.B., McSween, H.Y., Capaccioni, F., Capria, M.T., Carrozzo, F.G., Ciarniello, M., and others (2015) Ammoniated phyllosilicates with a likely outer Solar System origin on (1) Ceres. Nature, 528, 241–244.

De Sanctis, M.C., Mitri, G., Castillo-Rogez, J., House, C.H., Marchi, S., Raymond, C.A., and Sekine, Y. (2020) Relict Ocean Worlds: Ceres. Space Science Reviews, 216, 60, 33 pp.

Earley, J.W., Osthaus, B.B., and Milne, I.H. (1952) Purification and properties of montmorillonite. American Mineralogist, 38, 707–724.

Eggleton, R.A. (1977) Nontronite: chemistry and x-ray diffraction. Clay Minerals, 12, 181–194.

Ehlmann, B.L., Mustard, J.F., Murchie, S.L., Bibring, J.P., Meunier, A., Fraeman, A.A., and Langevin, Y. (2011) Subsurface water and clay mineral formation during the early history of Mars. Nature, 479, 53–60.

Fagel, N. (2007) Chapter Four Clay Minerals, Deep Circulation and Climate. Developments in Marine Geology, 1, 139–184.

Farmer, V.C., Russell, J.D., McHardy, W.J., Newman, A.C.D., Ahlrichs, J.L., and Rimsaite, J.Y. (1971) Evidence for loss of protons and octahedral iron from oxidized biotites and vermiculites. Mineralogical Magazine, 38, 121–137.

Fialips, C.I., Huo, D., Yan, L., Wu, J., and Stucki, J.W. (2002) Effect of Fe oxidation state on the IR spectra of Garfield nontronite. American Mineralogist, 87, 630–641.

Fox, V.K., Kupper, R.J., Ehlmann, B.L., Catalano, J.G., Razzell-hollis, J., Abbey, W.J., Schild, D.J., Nickerson, R.D., Peters, J.C., Katz, S.M., and others (2021) Synthesis and characterization of Fe(III)-Fe(II)-Mg-Al smectite solid solutions and implications for planetary science. American Mineralogist, 106, 964–982.

Fukushi, K., Sekine, Y., Sakuma, H., Morida, K., and Wordsworth, R. (2019) Semiarid climate and hyposaline lake on earty Mars inferred from reconstructed water chemistry at Gale. Nature Communications, 10, 4896.

Goodman, B.A., Russell, J.D., Fraser, A.R., and Woodhams, F.W.D. (1976) A Mössbauer and I.R. spectroscopic study of the structure of nontronite. Clays and Clay Minerals, 24, 53-59.

He, H., Li, T., Tao, Q., Chen, T., Zhang, D., Zhu, J., Yuan, P., and Zhu, R. (2014) Aluminum ion occupancy in the structure of synthetic saponites: Effect on crystallinity. American Mineralogist, 99, 109–116.

Johnston, J.H., and Cardile, C.M. (1987) Iron substitution in montmorillonite, illite, and glauconite by ^{57}Fe Mössbauer spectroscopy. Clays and Clay Minerals, 35, 170-176.

Köster, H.M., Ehrlicher, U., Gilg, H.A., Jordan, R., Murad, E., and Onnich, K. (1999) Mineralogical and Chemical Characteristics of Five Nontronites and Fe-rich Smectites. Clay Minerals, 34, 579–599.

Lauterbach, S., McCammon, C.A., Van Aken, P., Langenhorst, F., and Seifert, F. (2000) Mössbauer and ELNES spectroscopy of $(Mg,Fe)(Si,Al)O_3$ perovskite: A highly oxidised component of the lower mantle. Contributions to Mineralogy and Petrology, 138, 17-26.

Lee, K., Kostka, J.E., and Stucki, J.W. (2006) Comparisons of structural Fe reduction in smectites by bacteria and dithionite: An infrared spectroscopic study. Clays and Clay Minerals, 54, 195–208.

Mangold, N., Dehouck, E., Fedo, C., Forni, O., Achilles, C., Bristow, T., Downs, R.T., Frydenvang, J., Gasnault, O., L'Haridon, J., and others (2019) Chemical alteration of fine-grained sedimentary rocks at Gale crater. Icarus, 321, 619–631.

Michalski, J.R., Cuadros, J., Bishop, J.L., Darby Dyar, M., Dekov, V., and Fiore, S. (2015) Constraints on the crystal-chemistry of Fe/Mg-rich smectitic clays on Mars and links to global alteration trends. Earth and Planetary Science Letters, 427, 215–225.

Miyawaki, R., Sano, T., Ohashi, F., Suzuki, M., Kogure, T., Okumura, T., Kameda, J., Umezome, T., Sato, T., Chino, D., and others (2010) Some reference data for the JCSS clay specimens. Nendokagaku, 48, 158–198.

Moore, D.M., and Reynolds, Jr, R.C. (1997) X-ray diffraction and the identification and analysis of clay minerals, second., 378 p. Oxford University Press, Oxford.

Morris, R.V., Golden, D.C., Bell III, J.F., and Lauer Jr., H.V. (1995) Hematite, pyroxene, and phyllosilicates on Mars: Implications from oxidized impact melt rocks from Manicouagan Crater, Quebec, Canada. Journal of Geophysical Research, 100(E3), 5319-5328.

Nagelschmidt, G. (1938) On the atomic arrangement and variability of the members of the montmorillonite group. Mineralogical Magazine and Journal of the Mineralogical Society, 25, 140–155.

Prescher, C., McCammon, C., and Dubrovinsky, L. (2012) *MossA*: a program for analyzing energy-domain Mössbauer spectra from conventional and synchrotron sources. Journal of Applied Crystallography, 45, 329-331.

Russell, J.D., and Fraser, A.R. (1994) Infrared methods. In M.J. Wilson, Ed., Clay Mineralogy: Spectroscopic and Chemical Determinative Methods pp. 11–67. Chapman & Hall, London.

Shannon, R.D., and Prewitt, C.T. (1969) Effective ionic radii in oxides and fluorides. Acta Crystallographica Section B Structural Crystallography and Crystal Chemistry, 25, 925–946.

Stucki, J.W., Golden, D.C., and Roth, C.B. (1984) Preparation and Handling of Dithionite-Reduced Smectite Suspensions. Clays and Clay Minerals, 32, 191–197.

Sudo, T. (1954) Iron-rich saponite found from Tertiary iron sand beds of Japan (Reexamination on “Lembergite”). J. Geol. Soc. Japan, 60, 18–27.

Treiman, A.H., Morris, R. V., Agresti, D.G., Graff, T.G., Achilles, C.N., Rampe, E.B., Bristow, T.F., Blake, D.F., Vaniman, D.T., Bish, D.L., and others (2014) Ferrian saponite from the Santa Monica Mountains (California, U.S.A., Earth): Characterization as an analog for clay minerals on Mars with application to Yellowknife Bay in Gale Crater. American Mineralogist, 99, 2234–2250.

Vandenberghe, R.E., and De Grave, E. (2013) Application of Mössbauer Spectroscopy in Earth Sciences. In Y. Yoshida and G. Langouche, Eds., Mössbauer Spectroscopy pp. 91–185. Springer-Verlag, Berlin Heidelberg.

Vaniman, D.T., Bish, D.L., Ming, D.W., Bristow, T.F., Morris, R. V, Blake, D.F., Chipera, S.J., Morrison, S.M., Treiman, A.H., Rampe, E.B., and others (2014) Mineralogy of a Mudstone at Yellowknife Bay, Gale Crater, Mars. Science, 343, 1243480.

Weir, A.H., and Greene-Kelly, R. (1962) Beidellite. American Mineralogist, 47, 137–145.

Wilke, M., Farges, F., Petit, P.E., Brown, G.E., and Martin, F. (2001) Oxidation state and coordination of Fe in minerals: An Fe K-XANES spectroscopic study. American Mineralogist, 86, 714–730.

List of figure captions

Fig. 1. XRD profiles of precipitates (FS007, 009, and 010) and typical standard samples of synthetic saponite (Smecton SA), nontronite (NAu-1), and montmorillonite (Kunipia-F). The numbers indicate the *d*-spacing of smectite in Å. The Bragg reflections from basal planes were labeled as 00*l* without showing the *d*-spacing value, because the values vary depending on the humidity. Reflections originating from minor minerals were labeled as quartz (Qz), magnetite (Mag), and hematite (Hm).

Fig. 2. FTIR spectra of precipitates from three solutions with different Al contents. The arrows indicate the absorbance which is possibly related to the tetrahedral Al-O-Si vibrations (Russell and Fraser 1994).

Fig. 3. XRD profiles of FS009 and samples that were oxidized (FS009O), reduced for one hour (FS009R1h), and for 24 hours (FS009R24h). The reflections from magnetite and hematite were indicated by Mag and Hm, respectively.

Fig. 4. Low-resolution TEM images, ED patterns, and high-resolution TEM images of FS009O (a, b, c) and FS009R1h saponites (d, e, f). The ED patterns (b and e) were measured based on the TEM images (a and d).

Fig. 5. Fe K-edge XANES spectra of biotite, FS009R24h, FS009R1h, FS009O, and nontronite (NAu-1). Open circles indicate the energy of edge at the normalized absorbance of 0.5. Dashed lines indicate the minimum and maximum energies of edges in the measured samples. Low energy of edge corresponds to the high ratio of ferrous ion in the sample.

Fig. 6. Mössbauer spectra of (a) biotite, (b) FS009R24h, (c) FS009R1h, and (d) FS009O. Open circles are measured data. Solid line indicates the sum of each component from ferric and ferrous ions.

Fig. 7. Ferric iron/total iron ($Fe^{3+}/\Sigma Fe$) ratios in biotite and saponites estimated from the K-edge XANES spectra (open symbols) and from the Mössbauer spectra (solid symbols).

Fig. 8. A comparison of XRD profiles around 02*l* and 11*l* reflections among FS009O, FS009R24h, NAu-1, and two samples (John Klein and Cumberland) from the Yellowknife Bay in Gale crater (Vaniman et al. 2014).

Fig. 9. Relationship between d_{02l} and d_{060} for smectites (Mnt: montmorillonite (Nagelschmidt 1938; Earley et al. 1952; Miyawaki et al. 2010), Fe-rich Mnt (Fox et al. 2021), Bei: beidellite (Nagelschmidt 1938; Weir and Greene-Kelly 1962), Non: nontronite (Nagelschmidt 1938; Eggleton 1977; Our sample), Mg-Sap: Mg-saponite (Nagelschmidt 1938; Cahoon 1954; Miyawaki et al. 2010), Di-trioctahedral Fe-Sme: Di-trioctahedral Fe-smectite (Fox et al. 2021), Fe-Sap: Fe-saponite (Sudo 1954; Baldermann et al. 2014; Chemtob et al. 2015; Fox et al. 2021). Open and solid symbols are categorized to di-octahedral and tri-octahedral smectites, respectively. Solid line indicates the ideal correlation described as $d_{02l} = 3d_{060}$. Shaded zone indicates the d_{02l} values of smectites found in the Yellowknife Bay. Our data includes several synthesized samples of Fe-Sap in addition to FS007, FS009, and FS010.

Fig. 10. Iron content in octahedral sheets (Fe_{Oct}) in a half-unit cell versus lattice parameter *b*.

The abbreviations of mineral names are the same as those in Fig. 9. Dashed and solid lines indicate the fitted linear lines to open and solid symbols, respectively. Shaded zone indicates the estimated range in the *b* parameter of smectites found in Yellowknife Bay.

Table 1. Molar ratio of elements in the initial solutions.

Element	FS007	FS009	FS010
Si	3.49	3.69	4.00
Mg	1.51	1.51	1.49
Fe	1.51	1.50	1.50
Al	0.50	0.30	0.00

Table 2. Estimated oxide concentration in trioctahedral smectites.

Oxide (wt%)	FS007	FS009	FS010
Na_2O	4.2	3.2	2.8
MgO	11.4	11.9	11.8
Al_2O_3	9.8	5.7	0.0
SiO_2	35.7	37.4	38.3
FeO	22.8	20.5	17.9
Fe_2O_3	3.0	4.4	6.9
H_2O	13.1	16.8	22.4

Table 3. Calculated chemical formula of trioctahedral smectites.

Sample	**Chemical formula**
FS009	$Na_{0.54}(Mg_{1.53}Fe_{1.47})(Si_{3.22}Al_{0.57}Fe_{0.29})O_{10}(OH)_2$
FS010	$Na_{0.50}(Mg_{1.61}Fe_{1.38})(Si_{3.52}Fe_{0.48})O_{10}(OH)_2$

Table 4. Estimated $Fe^{3+}/\Sigma Fe$ by XANES spectra. The range in biotite was obtained by measuring several samples.

Sample	**$Fe^{3+}/\Sigma Fe$**
Biotite	0.09 ± 0.06
FS009R24h	0.35 ± 0.06
FS009R1h	0.29 ± 0.06
FS009O	0.69 ± 0.06

619 **Table 5. Mössbauer parameters at room temperature**

Sample	Cation	IS[a] (mm/s)	QS[b] (mm/s)	FWHM[c] (mm/s)	Area (%)[d]	$Fe^{3+}/\Sigma Fe$[e]
FS009O	Fe^{2+}	1.00 (7)[f]	2.70 (14)	0.27 (21)	12 (7)	0.86 (8)
	Fe^{3+}	0.32 (3)	0.82 (5)	0.48 (7)	88 (7)	
FS009R1h	Fe^{2+}	1.10 (2)	2.62 (4)	0.25 (5)	34 (7)	0.62 (21)
	Fe^{3+} (Oct)[g]	0.35 (5)	0.77 (8)	0.45 (11)	53 (9)	
	Fe^{3+} (Tet)[h]	0.05 (14)	0.30 (28)	0.36 (38)	13 (10)	
FS009R24h	Fe^{2+}	1.13 (3)	2.51 (6)	0.33 (6)	23 (4)	0.73 (15)
	Fe^{3+} (Oct)	0.34 (2)	1.02 (7)	0.57 (6)	69 (6)	
	Fe^{3+} (Tet)	0.27 (6)	0.35 (11)	0.31 (23)	8 (7)	
Biotite	Fe^{2+}	1.11 (1)	2.51 (1)	0.47 (1)	90 (2)	0.09 (4)
	Fe^{3+} (Oct)	0.50 (11)	0.60 (15)	0.48 (22)	6 (2)	
	Fe^{3+} (Tet)	−0.04 (3)	0.35 (7)	0.20 (7)	4 (1)	
Constraints[i]	Fe^{2+}	1-1.2	1.6-3.2	0.2-1		
	Fe^{3+}	−0.2-0.5	0.2-1.3	0.2-1		

Fe^{3+} (Oct)	0.25-0.5	0.2-1.3	0.2-1
Fe^{3+} (Tet)	−0.2-0.3	0-0.35	0.2-1

[a] IS = isomer shift. [b] QS = quadrupole splitting. [c] FWHM = full width at a half-maximum. [d] Uncorrected Area by the recoilless fraction. [e] Calculated by using the recoilless fraction ratio of 1.21. [f] Number in parentheses represent fitting uncertainty for final digit(s). [g] Ferric ion in octahedral site. [h] Ferric ion in tetrahedral site. [i] Constraints in the fit range of parameters.

Table 6. Calculated chemical formula of oxidized and reduced FS009.

Sample	**Chemical formula**
FS009O	$Na_{0.43}(Mg_{1.70}Fe(II)_{0.54}\ Fe(III)_{0.76})(Si_{3.27}Al_{0.39}Fe_{0.43})O_{10.80}(OH)_{1.20}$
FS009R1h	$Na_{0.51}(Mg_{2.01}Fe(II)_{0.85}\ Fe(III)_{0.14})(Si_{3.36}Al_{0.47}Fe_{0.21})O_{10.18}(OH)_{1.82}$

Figure 1

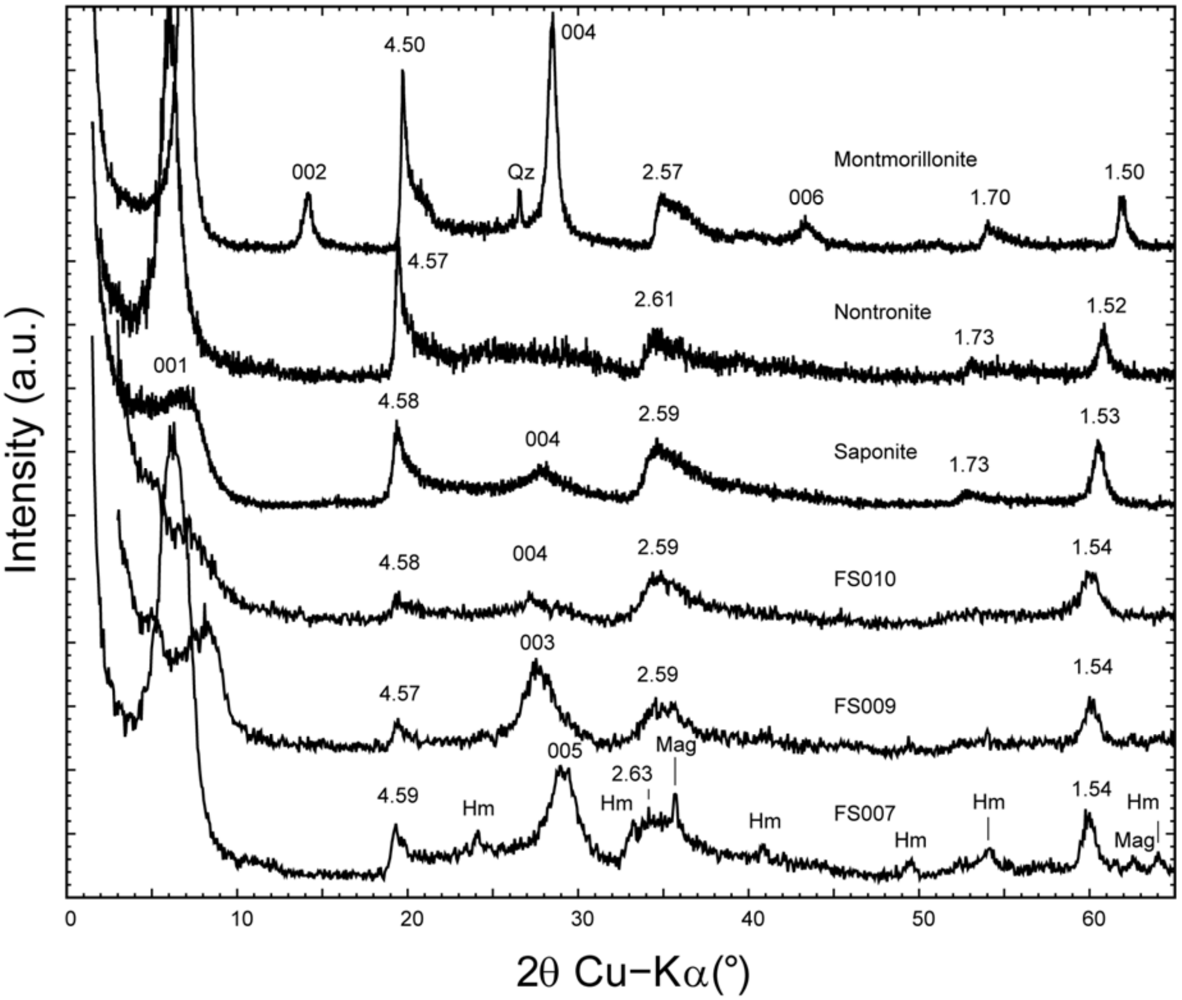

Figure 1 XRD profiles of precipitates (FS007, 009, and 010) and typical standard samples of synthetic saponite (Smecton SA), nontronite (NAu-1), and montmorillonite (Kunipia-F). The numbers indicate the *d*-spacing of smectite in Å. The Bragg reflections from basal planes were labeled as 00*l* without showing the *d*-spacing value, because the values vary depending on the humidity. Reflections originating from minor minerals were labeled as

quartz (Qz), magnetite (Mag), and hematite (Hm).

Figure 2

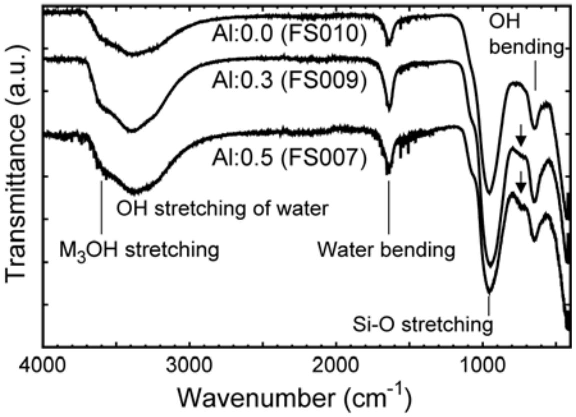

Figure 2 FTIR spectra of precipitates from three solutions with different Al contents. The arrows indicate the absorbance which is possibly related to the tetrahedral Al-O-Si vibrations (Russell and Fraser 1994).

Figure 3

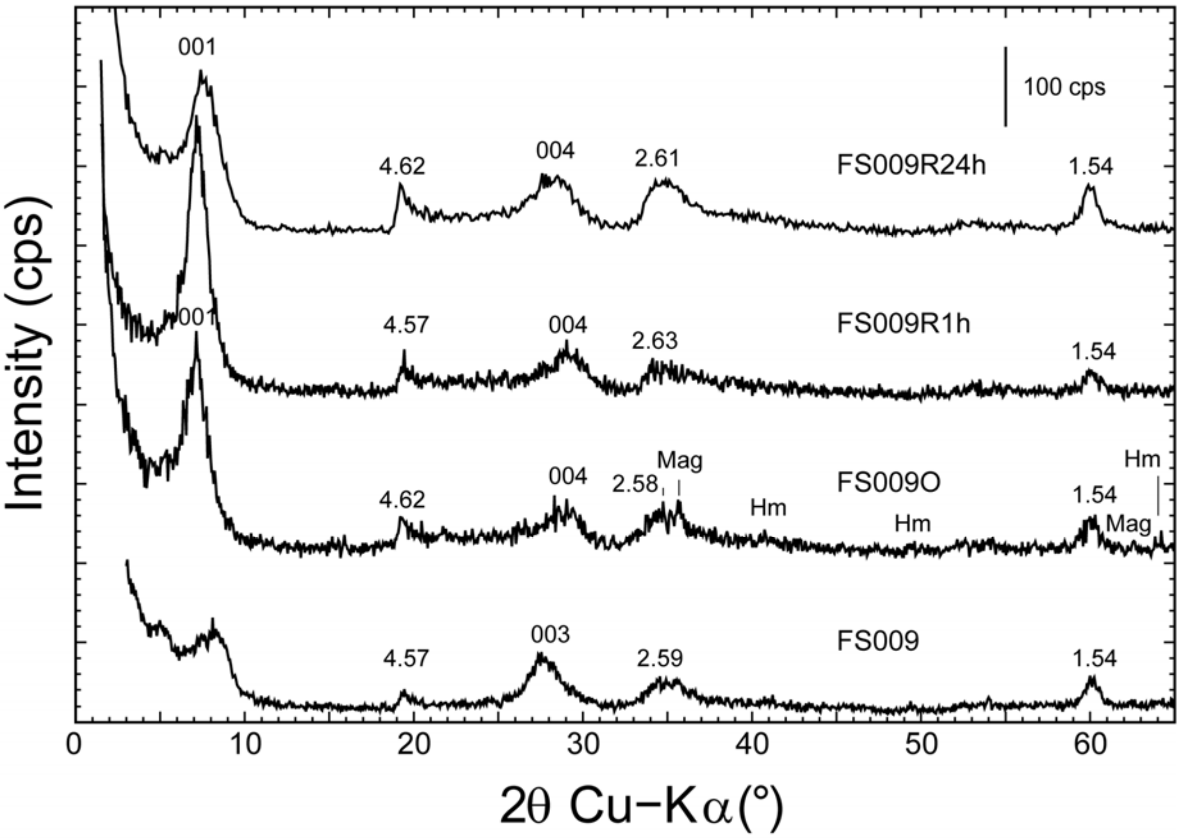

Figure 3 XRD profiles of FS009 and samples that were oxidized (FS009O), reduced for one hour (FS009R1h), and for 24 hours (FS009R24h). The reflections from magnetite and hematite were indicated by Mag and Hm, respectively.

Figure 4

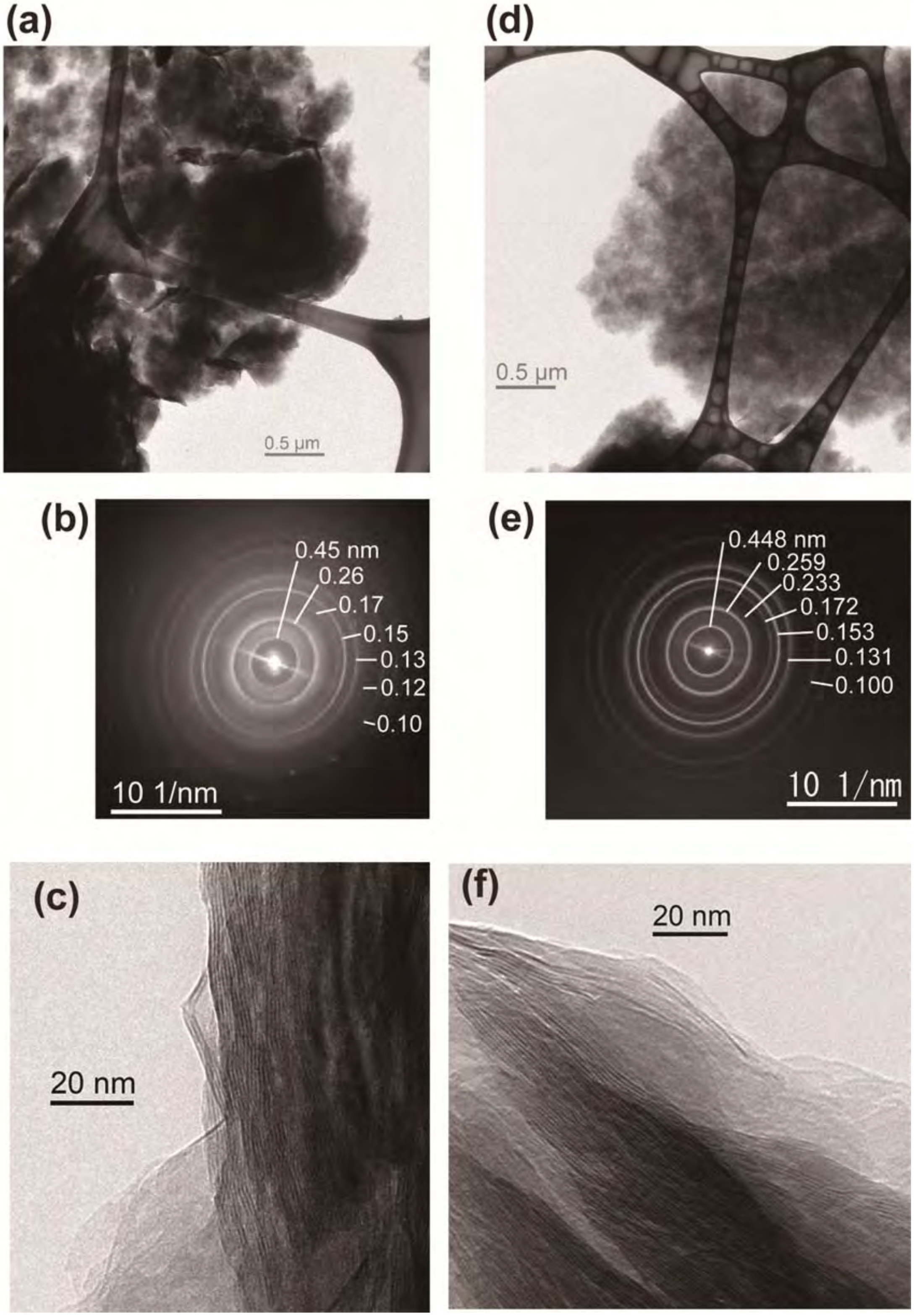
(a)
0.5 μm
(d)
0.5 μm
(b)
0.45 nm
0.26
0.17
0.15
0.13
0.12
0.10
10 1/nm
(e)
0.448 nm
0.259
0.233
0.172
0.153
0.131
0.100
10 1/nm
(c)
20 nm
(f)
20 nm

Figure 4 Low-resolution TEM images, ED patterns, and high-resolution TEM images of FS009O (a, b, c) and FS009R1h saponites (d, e, f). The ED patterns (b and e) were measured based on the TEM images (a and d).

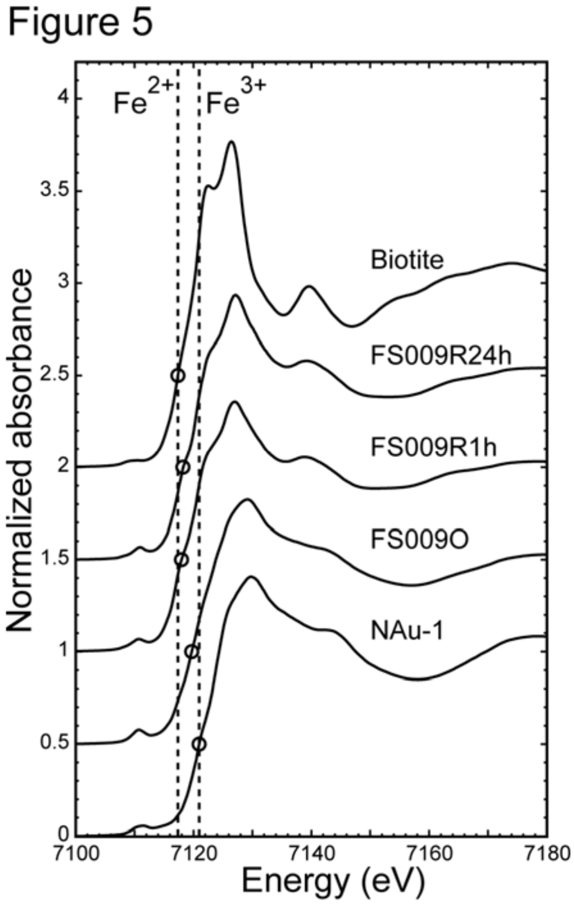

Figure 5 Fe K-edge XANES spectra of biotite, FS009R24h, FS009R1h, FS009O, and nontronite (NAu-1). Open circles indicate the energy of edge at the normalized absorbance of 0.5. Dashed lines indicate the minimum and maximum energies of edges in the measured samples. Low energy of edge corresponds to the high ratio of ferrous ion in the sample.

Figure 6

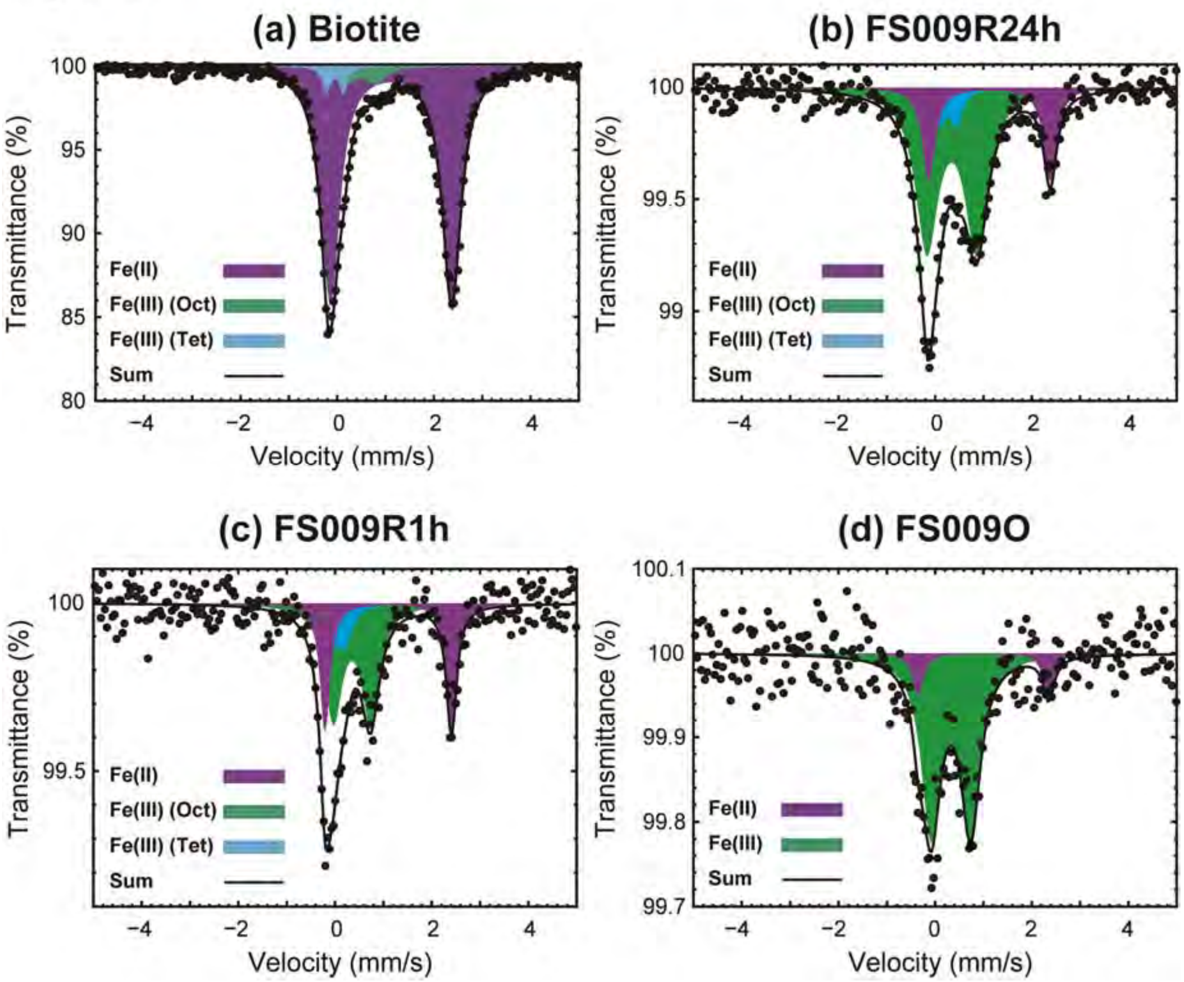

Figure 6 Mössbauer spectra of (a) biotite, (b) FS009R24h, (c) FS009R1h, and (d) FS009O. Open circles are measured data. Solid line indicates the sum of each component from ferric and ferrous ions.

Figure 7

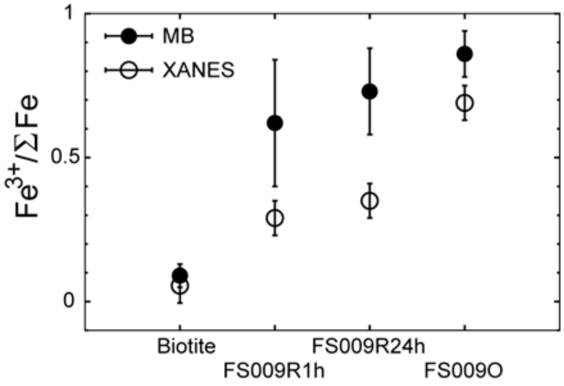

Figure 7 Ferric iron/total iron (Fe^{3+}/Σ Fe) ratios in biotite and saponites estimated from the K-edge XANES spectra (open symbols) and from the Mössbauer spectra (solid symbols).

Figure 8

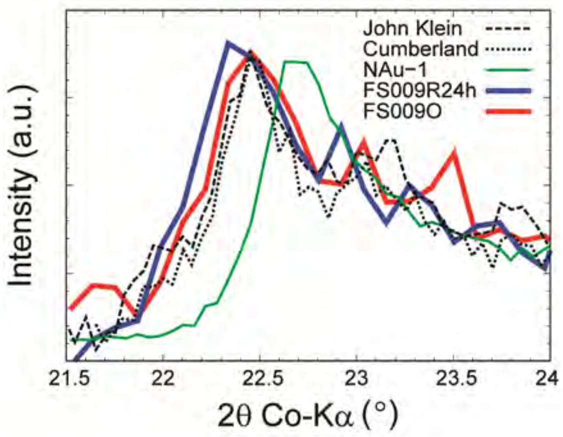

Figure 8 A comparison of XRD profiles around 02*l* and 11*l* reflections among FS009O, FS009R24h, NAu-1, and two samples (John Klein and Cumberland) from the Yellowknife Bay in Gale crater (Vaniman et al. 2014).

Figure 9

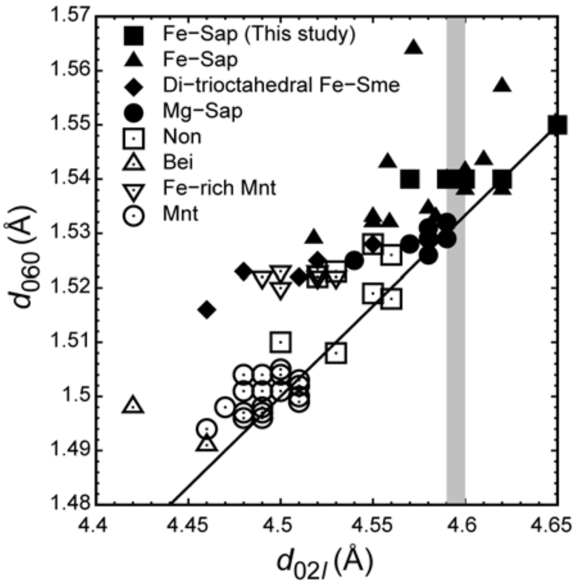

Figure 9 Relationship between d_{02l} and d_{060} for smectites (Mnt: montmorillonite (Nagelschmidt 1938; Earley et al. 1952; Miyawaki et al. 2010), Fe-rich Mnt (Fox et al. 2021), Bei: beidellite (Nagelschmidt 1938; Weir and Greene-Kelly 1962), Non: nontronite (Nagelschmidt 1938; Eggleton 1977; Our sample), Mg-Sap: Mg-saponite (Nagelschmidt 1938; Cahoon 1954; Miyawaki et al. 2010), Di-trioctahedral Fe-Sme: Di-trioctahedral Fe-smectite (Fox et al. 2021), Fe-Sap: Fe-saponite (Sudo 1954; Baldermann et al. 2014; Chemtob et al. 2015; Fox et al. 2021). Open and solid symbols are categorized to di-octahedral and tri-octahedral smectites, respectively. Solid line indicates the ideal correlation described as $d_{02l} = 3d_{060}$. Shaded zone indicates the d_{02l} values of smectites found in the Yellowknife Bay. Our data includes several synthesized samples of Fe-Sap in addition to FS007, FS009, and FS010.

Figure 10

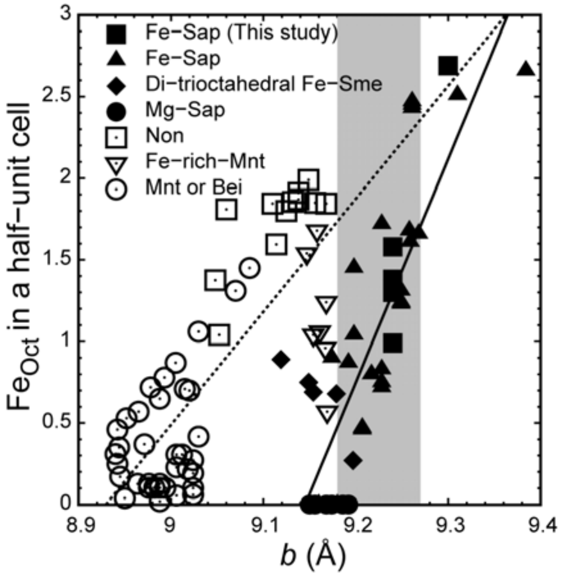

Figure 10 Iron content in octahedral sheets (Fe_{Oct}) in a half-unit cell versus lattice parameter *b*. The abbreviations of mineral names are the same as those in Fig. 9. Dashed and solid lines indicate the fitted linear lines to open and solid symbols, respectively. Shaded zone indicates the estimated range in the *b* parameter of smectites found in Yellowknife Bay.